ACS APPLIED MATERIALS & INTERFACES

Research Article

www.acsami.org

Electrochemical Capacitance of Ni-Doped Metal Organic Framework and Reduced Graphene Oxide Composites: More than the Sum of Its Parts

Parama Chakraborty Banerjee, Derrek E. Lobo, Rick Middag, Woo Kan Ng, Mahdokht E. Shaibani, and Mainak Majumder*

Nanoscale Science and Engineering Laboratory (NSEL), Department of Mechanical and Aerospace Engineering, Monash University, Clayton, Victoria 3800, Australia

Supporting Information

ABSTRACT: Composites of a Ni-doped metal organic framework (MOF) with reduced graphene oxide (rGO) are synthesized in bulk (gram scale) quantities. The composites are composed of rGO sheets, which avoid restacking from the physical presence of MOF crystals. At larger concentration of rGO, the MOF crystals are distributed on the overlapping and continuous rGO sheets. Ni in Ni-doped MOF is found to engage in a two-electron, reversible, efficient, redox reaction shuttling between Ni and $Ni(OH)_2$ in aqueous potassium hydroxide (KOH) electrolyte. The reaction is rather unique as Ni-based supercapacitors use a one-electron transfer Faradaic redox reaction between $Ni(OH)_2$ and NiO-(OH). Employing electrochemical impedance spectroscopy, we determined the charge transfer resistance to be 184 mΩ for MOF, 74 mΩ for a Ni-doped MOF and 6 mΩ for a rGO−Ni-doped MOF composite, but these modifications do not affect the mass transfer resistance. This novel redox reaction in conjunction with the lowered charge transfer resistance from the introduction of rGO underpins the synergy that dramatically increases the capacitance to 758 F/g in the rGO−Ni-doped MOF composite, when the parent MOF could store only 100 F/g and a physical composite of rGO and Ni-doped MOF could algebraically achieve about 240 F/g. A generic approach of doping MOFs with a redox active metal and forming a composite with rGO transforms an electro-inactive MOF to high capacity energy storage material with energy density of 37.8 Wh/kg at a power density of 227 W/kg. These results can promote the development of high-performance energy storage materials from the wide family of MOFs available.

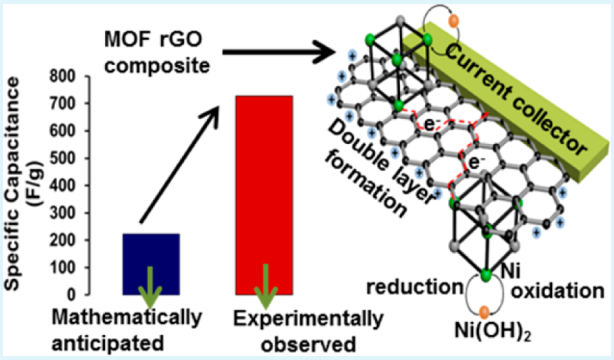

KEYWORDS: *graphene, supercapacitor, MOF, electrochemistry*

1. INTRODUCTION

Ever growing demand for power systems for delivering energy at high power has necessitated the application of supercapacitors as charge storage devices. Supercapacitors can store energy by non-Faradaic process in which charges are stored electrostatically at the electrode interfaces or by Faradaic process in which charge storage is accomplished by electron transfer through changes in the oxidation state of electrode material. Depending on the electrode material, these two mechanisms can operate independently or together. Faradaic redox reactions depend on reactant ions and reaction site density can provide 10−100 times higher energy density than non-Faradaic processes,[1] while double layer charging usually provides high power density. So, materials that combine both Faradaic and non-Faradaic processes are likely to provide optimal combination of energy and power density.

Metal organic frameworks (MOFs) are crystalline, open-porous materials consisting of metal ions or metal−oxo units coordinated by electron donating organic ligands and possess very high surface area (~7000 m^2/g),[2] well-defined pore sizes, tailorable structure and permeability to guest molecules.[3−5] They have found application in catalysis,[6] gas separation,[7] drug storage and delivery,[8,9] imaging and sensing,[10] optoelectronics[11] and molecular sieving.[5] MOFs with different metal centers and tunable organic ligands have been synthesized, and while these chemical building blocks can participate in electron exchange processes with the likelihood of providing rich fundamental data, utilizing these materials for energy storage application has been limited. The electrochemistry of MOFs would involve several coupled processes of electron transfer and ion transport into/from the solid lattice.[12−14] In an early report, Doménech et al.[15] showed that Cu MOF and Zn MOF underwent well-defined reduction processes depending on the type of electrolyte, followed by oxidative dissolution of

Received: November 19, 2014
Accepted: January 23, 2015
Published: January 23, 2015

ACS Publications © 2015 American Chemical Society

DOI: 10.1021/am508119c
ACS Appl. Mater. Interfaces 2015, 7, 3655−3664

electrochemically generated metal deposits. Loera-Serna et al.[16] reported that the synthesis process determines the Cu content in the resultant HKUST1MOF ($Cu_3(BTC)_2$; BTC = 1,3,5-benzenetricarboxylate), so HKUST1 prepared by various synthesis methods elicit Faradaic reactions to different degree. Lee et al.[17] reported high capacitance for Co MOF in the presence of lithium hydroxide (LiOH), however it became unstable in aqueous potassium hydroxide (KOH). Díaz et al.[18] synthesized Co-doped MOF-5 and evaluated its electrochemical performance using 0.1 M tetrabutylammonium hexafluorophosphate ($TBAPF_6$) in acetonitrile, achieving a maximum capacitance of a modest 2 F/g, likely because the metal centers did not participate in any Faradaic reaction. Moreover MOFs are inherently insulators that potentially limit their capacity to deliver power. Thus, composites of MOF with nanoscale conductive phases such as graphene are a realistic strategy for improving the power densities of MOF-based materials. Reduced graphene oxide (rGO) possesses high conductivity and high surface area and has been exploited as an electrical double-layer supercapacitor.[19] Reports related to MOF/graphene oxide (GO) and MOF/rGO composites so far focused on applications in gas adsorption,[20,21] electrochemical biosensing,[22] photocatalysis, and gas sensing.[23] Recently, however, Choi et al.[24] have demonstrated the possibility of MOFs in electrochemical energy storage by studying a series of MOFs as a composite with graphene for energy storage applications. The highest capacitance (0.64 F/cm^3_{stack} and 5.09 mF/cm^2) was reported for a Zr and 4,4′-biphenyldicarboxylate MOF/graphene composite in 1 M tetraethylammonium tetrafluoroborate ($(C_2H_5)_4NBF_4$).

Discovering novel MOFs with excellent energy storage capabilities could be serendipity, but tailoring existing MOF and encouraging the metal centers to participate in rapid electron transfer processes mediated by the graphene nanosheets would be a generic approach to obtain new high-performance, next-generation energy storage materials. We have therefore investigated the effect of doping of Ni into the lattice of a prototypical MOF structure, MOF-5, and the formation of intimately mixed composites with rGO on the electrochemical charge storage capability and mechanisms. In general, MOF-5 suffers from poor electrochemical response and instability in aqueous media because the Zn metal centers undergo irreversible redox processes in most aqueous electrolytes over the general operating potential window (0−1 V).[25] Our strategy (illustrated in Scheme 1) relies on partially substituting the Zn metal centers with Ni, which is known to make the MOF-5 stable in aqueous environments and undergo reversible redox reactions in the presence of alkaline electrolytes. Forming a composite with rGO is expected to increase the electronic conductivity, which would enhance charge transfer characteristics.

Scheme 1. Concept for Ni Doping and Incorporating rGO to Form a Composite of rGO and Ni-doped MOF-5 and Its Use As an Electrode Material That Harness Both the Electrochemical Double Layer Performance of rGO and the Reversible Redox Reactions of Ni Metal Centers with a Synergy That Facilitates Effective and Efficient Charge Transfer Processes

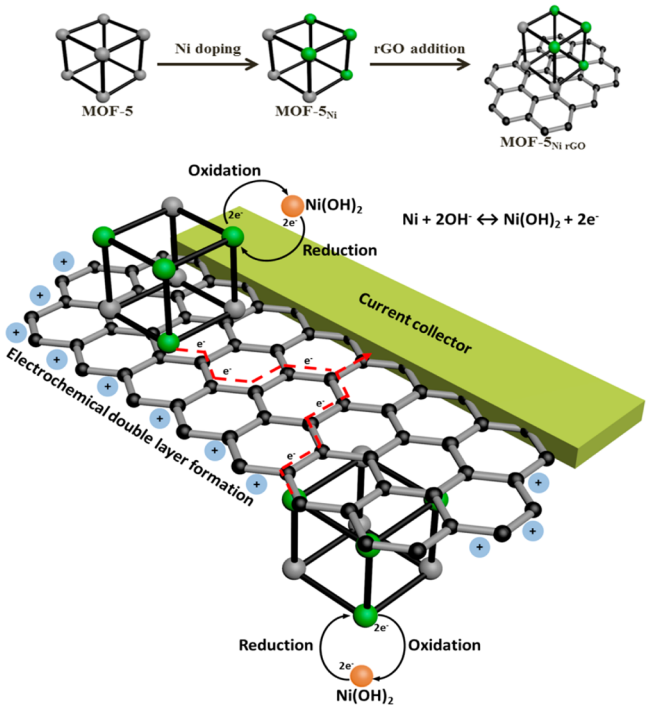

2. EXPERIMENTAL METHODS

2.1. Synthesis of MOF-5, rGO, Ni-Doped MOF-5 (MOF-5_{Ni}) and rGO Added Ni-Doped MOF-5 (MOF-$5_{Ni\ rGO}$). All reagents, unless otherwise stated, were obtained from commercial sources (Sigma-Aldrich, Merck, and Ajax Fine Chemicals, Pty., Ltd.). They were of analytical grade and were used without any further purification.

2.1.1. MOF Synthesis. Published procedures[26−28] have been followed to synthesize MOF-5. Briefly, 1.2 g of zinc nitrate hexahydrate ($Zn(NO_3)_2$, $6H_2O$) and 0.334 g of terephthalic acid (BDC, $C_6H_4(COOH)_2$) were dissolved in a solution of 40 mL of dimethylformamide (DMF) and 5 mL of Chlorobenzene under constant stirring. Subsequently, 2.2 mL of triethylamine (TEA) and 4 drops of hydrogen peroxide (H_2O_2) were added, and the mixture was subjected to agitation for 45 min. The resultant white precipitate was collected by vacuum filtration and was washed with DMF (3 × 10 mL). The filtrate material was stored in chloroform ($CHCl_3$) for 24 h to exchange DMF solution.

Ni-doped MOFs were synthesized using the same procedure as MOF-5 synthesis. However, in this case, $Zn(NO_3)_2$, $6H_2O$ was partially substituted by nickel nitrate hexahydrate ($Ni(NO_3)_2$, $6H_2O$). For example, to synthesize 50% Ni doped MOF-5, we used 0.6 g of $Ni(NO_3)_2$, $6H_2O$ along with 0.6 g of $Zn(NO_3)_2$, $6H_2O$. The Ni-doped MOF-5 would henceforth be known as MOF-5_{Ni}.

2.1.2. rGO Synthesis. Graphene oxide (GO), the precursor for reduced graphene oxide (rGO) was synthesized from natural graphite powder (provided by SER, Pty., Ltd.) using a modified Hummers method.[29] Details of GO synthesis is reported in the Supporting Information (Section S1). A procedure reported by Stankovich et al.[30] was used to reduce as prepared GO. In a typical process, 100 mg of GO was loaded in a round-bottom flask, and 100 mL of water was added. The resultant inhomogeneous brown dispersion was then sonicated in an ultrasonic bath cleaner for 1 h. Then, 1 mL of hydrazine hydrate (32 mmol) was added to the GO dispersion and the mixture was heated at 100 °C for 24 h under a water cooled condenser. The black precipitate was isolated under vacuum filtration using a 0.2 μm nylon filter. The filtrate was collected, copiously washed with distilled water (5 × 100 mL) and methanol (5 × 100 mL), and dried under a continuous flow of air.

2.1.3. MOF rGO Composite. To synthesize the MOF rGO composites, we dispersed different weight percentages (5, 10, 30, and 50%) of rGO in a mixture of DMF and chlorobenzene, which was used during the synthesis of MOF-$5_{Ni50\%}$. In a typical process, 0.76 g of rGO (which is 50% of the total weight of the metal nitrate salt and BDC) was dispersed in 40 mL of DMF, and the mixture was sonicated in an ultrasonic bath cleaner for 5 h. Subsequent centrifugation at 3000

DOI: 10.1021/am508119c
ACS Appl. Mater. Interfaces 2015, 7, 3655−3664

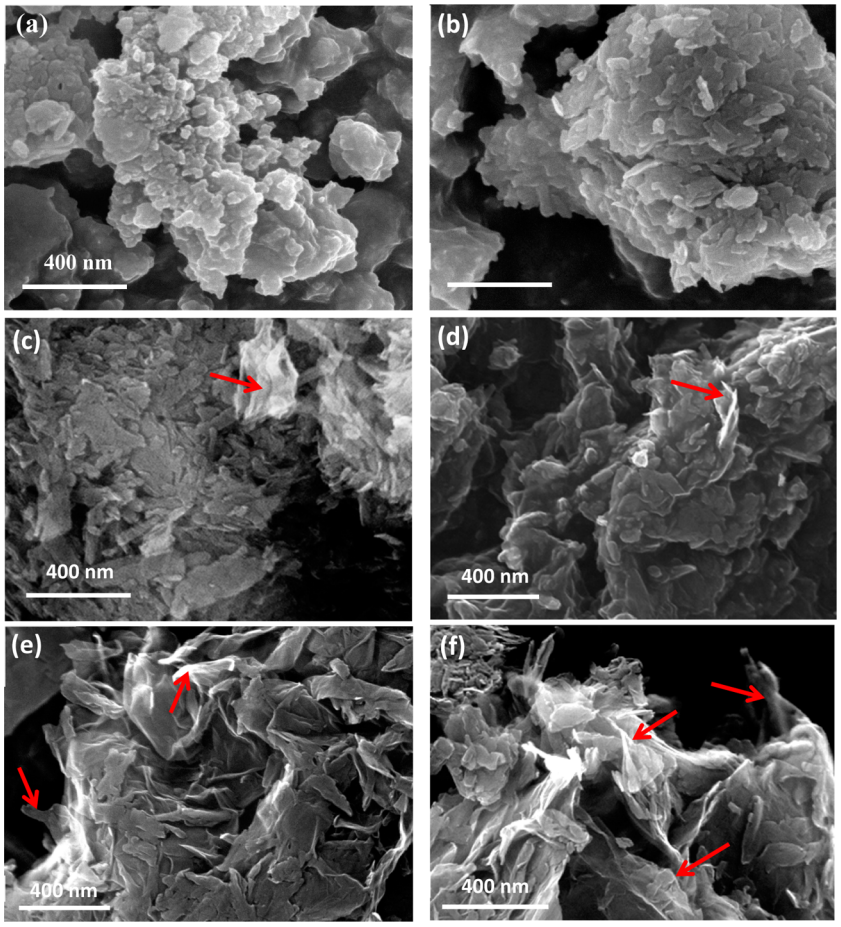

Figure 1. SEM micrographs of (a) MOF-5 and (b) MOF-$5_{Ni50\%}$. Little change in the flake-like morphology of MOF-5 occurred due to Ni doping. SEM micrographs of (c) MOF-$5_{Ni50\%\ rGO5\%}$, (d) MOF-$5_{Ni50\%\ rGO10\%}$, (e) MOF-$5_{Ni50\%\ rGO30\%}$, and (f) MOF-$5_{Ni50\%\ rGO50\%}$.

rpm for 10 min did not show presence of any aggregates, which indicated that rGO sheets were well dispersed in DMF. Subsequently, 5 mL of chlorobenzene was added to this well-dispersed rGO dispersion, and the dispersion was kept under constant stirring. Next, 0.6 g of $Ni(NO_3)_2$, $6H_2O$, 0.6 g $Zn(NO_3)_2$, $6H_2O$, and 0.334 g BDC were dissolved in the rGO/DMF/chlorobenzene dispersion. Further, 2.2 mL of TEA and 4 drops of H_2O_2 were added, and the mixture was agitated for 45 min. The resultant black precipitate was collected by vacuum filtration and was washed with DMF (3 × 10 mL). The black filtrate was stored in chloroform ($CHCl_3$) for 24 h to exchange DMF solution. This procedure was repeated to synthesize various MOF rGO composites with different weight percentages (5, 10, and 30%) of rGO. The rGO incorporated MOF-$5_{Ni50\%}$ would henceforth be known as MOF-$5_{Ni50\%\ rGO}$.

2.2. Characterization of MOF-5, MOF-5_{Ni}, and MOF-$5_{Ni50\%\ rGO}$

2.2.1. Scanning Electron Microscopy (SEM), Transmission Electron Microscopy (TEM), and Energy Dispersive X-ray (EDX) Analyses. The morphologies of the MOF samples were analyzed by a FEI Nova NanoSEM 450 FEGSEM. To avoid charging, we coated all MOF samples with a thin layer of gold prior to SEM analysis. TEM analysis was performed using an FEI Tecnai G2 T20 TWIN TEM at 200 keV. MOF-$5_{Ni50\%}$ and the MOF-$5_{Ni50\%\ rGO50\%}$ samples were dispersed in ethanol and loaded on a holey carbon-cupper grid. EDX analysis was performed with a Bruker Quantus 200 TEM X-ray analysis system and 30 mm^2 SDD with super light element window (slew) fitted with the FEI Tecnai G2 T20 TWIN TEM. During the EDX analysis, the sample was tilted at 20°.

2.2.2. X-ray Diffraction (XRD) Analysis. MOF and MOF rGO composites were analyzed by XRD using a Phillips 1140 diffractometer with Cu Kα line generated at 40 kV and 25 mA at a scan rate of 0.5°/min and a step size of 0.02°.

2.2.3. Raman Spectroscopy Analysis. Raman spectra were obtained using a Renishaw Confocal micro-Raman Spectrometer equipped with a HeNe (632.8 nm) laser operating at 10% power. Extended scans (10 s) were performed between 100 and 3200 wave numbers with a laser spot size of 1 μm. Once the background was removed, the intensity of the spectra was normalized by dividing the data with the maximum intensity. The peak position was found using the full width at half-maximum, as is common practice for analyzing spectral data.

2.2.4. Surface Area and Pore Textural Characterization. Surface area and pore textural characteristics of the $MOF_{Ni50\%}$ and $MOF_{Ni50\%\ rGO50\%}$ were obtained from the N_2 adsorption isotherms for pressures up to 1 bar measured by a volumetric method using a Micromeritics ASAP 2420 instrument at 77 K (liquid nitrogen bath). Freshly prepared samples were transferred into a predried, evacuated, and weighed Braunauer–Emmett–Teller (BET) analysis tube. Samples were evacuated and activated at 200 °C under dynamic vacuum at 10^{-6} Torr for 12 h to remove any residual solvent and measure the sample mass precisely. Gas adsorption measurements were performed using ultrahigh purity nitrogen. BET surface area and pore size distribution data were calculated from the N_2 adsorption isotherms based on the DFT model in the software provided within the Micromeritics ASAP 2420 instrument.

2.2.5. Electrical Conductivity Measurements. Conductivity was measured by an Agilent B2902A source measuring unit (SMU) with Agilent Quick IV software. The current was measured as the electrode potential was swept from −0.05 to +0.05 V. The scan rate used in the measurements was 0.022 V/s with a measurement taken at every 0.0001 V. The details of the process and formula used to calculate conductivity is elaborated in the Supporting Information (section S2).

DOI: 10.1021/am508119c
ACS Appl. Mater. Interfaces 2015, 7, 3655−3664

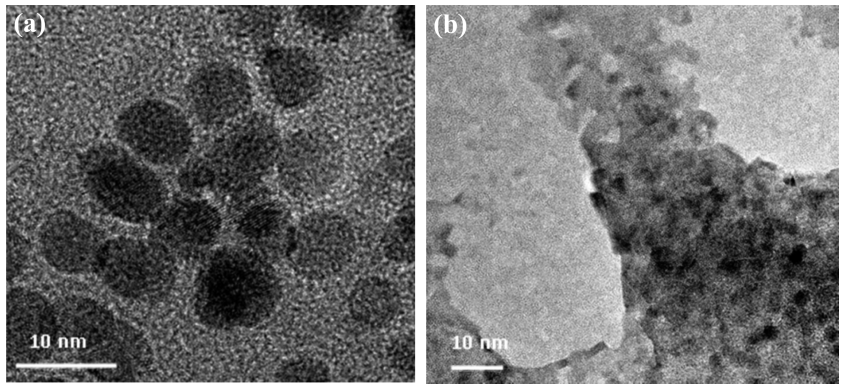

Figure 2. TEM micrographs of (a) MOF-$5_{Ni50\%}$ on holey carbon−copper grid and (b) MOF-$5_{Ni50\%\ rGO50\%}$ showing MOF-$5_{Ni50\%}$ distributed on rGO sheets.

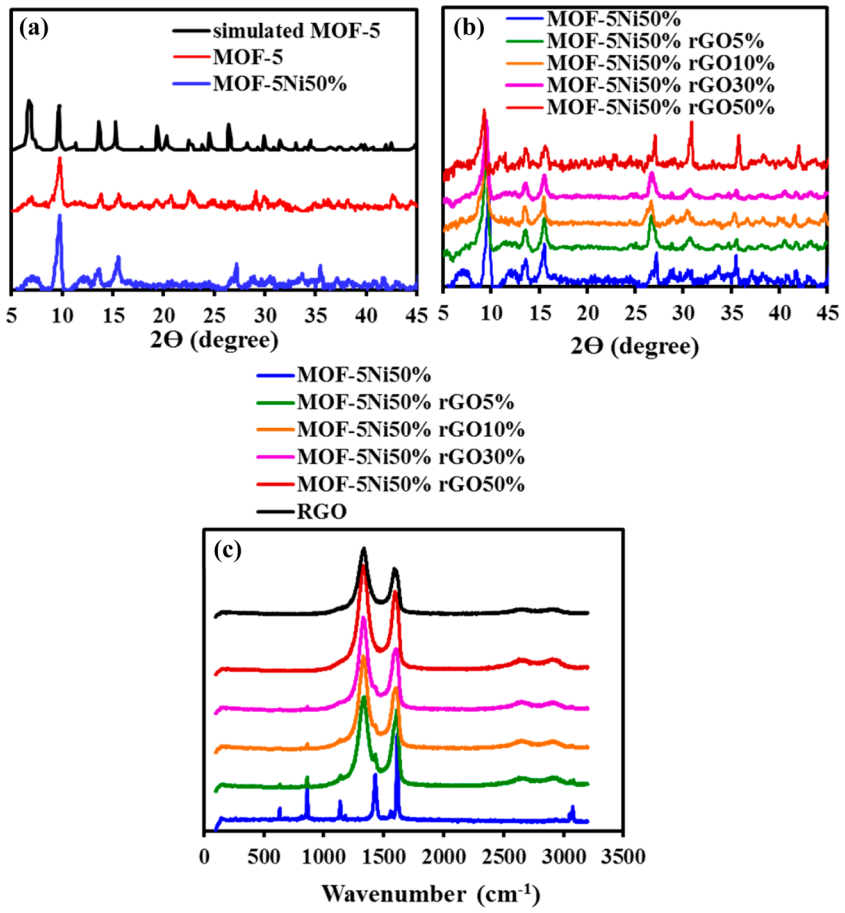

Figure 3. XRD spectra of (a) simulated MOF-5, MOF-5 and MOF-$5_{Ni50\%}$. (b) XRD and (c) Raman spectra of MOF-$5_{Ni50\%}$ with and without rGO addition. Relative comparison of the Raman spectra of rGO and MOF-$5_{Ni50\%\ rGO}$ confirmed the presence of few layer thin rGO in the composites.

2.2.6. Fabrication of the Electrodes for Electrochemical Measurements. The as-prepared MOF and MOF−rGO composites, acetylene black, and polyvinylidene difluoride (PVDF), were mixed in a mass ratio of 80:10:10 and dispersed in *N*-methyl-2-pyrrolidone (NMP). Then, the resultant mixture was coated on a 10 mm diameter titanium (Ti) disk with a doctor blade. This procedure was followed by drying the electrodes at room temperature for 24 h. The average thickness of the electroactive material coated on the Ti current collector was ∼55 μm, as measured by a Dektak 150 profilometer.

2.2.7. Electrochemical Measurements. All the electrochemical measurements were performed in 1 M potassium hydroxide (KOH; Merck) using a BioLogic VSP potentiostat and an electrochemical cell containing three electrodes (the prepared electrodes acted as the working electrode, platinum mesh and silver/silver chloride electrode (Ag/AgCl) were used as the counter and the reference electrodes, respectively). All the measurements were performed under ambient conditions. Open-circuit potential measurements were performed for 1 h prior to every electrochemical experiment to ensure a stable electrochemical condition. A fluctuation of less than 10 mV of the open circuit potential sustained for a period of 1000 s was considered as a stable electrochemical condition. Cyclic voltammetry (CV) measurements were performed between 0 and 0.6 V (vs Ag/AgCl) at a scan rate of 1 mV/s for 5 cycles. To obtain consistent measurements, we monitored the change in the current responses over different cycles. We observed no significant change in the CV plots after the second cycle, and hence, the CV plots reported here are the ones

DOI: 10.1021/am508119c
ACS Appl. Mater. Interfaces 2015, 7, 3655−3664

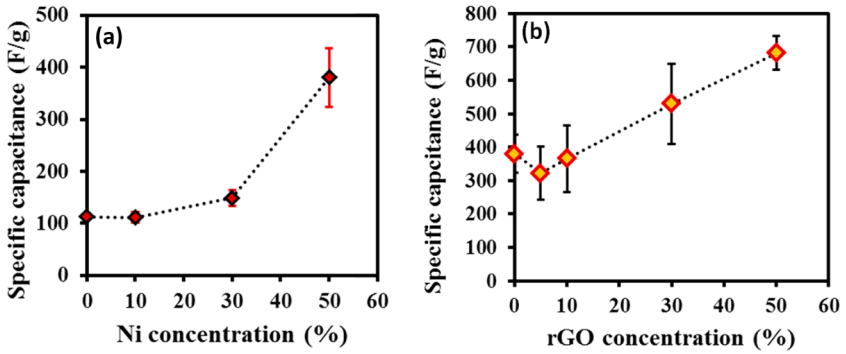

Figure 4. (a) Specific capacitance as a function of Ni doping concentration and (b) specific capacitance as a function of rGO concentration in MOF-$5_{Ni50\%}$ in 1 M KOH.

obtained after the third cycle. The formula used to calculate specific capacitances, energy, and power densities of the electrodes are elaborated in the Supporting Infromation (section S3.1). Galvanostatic charge/discharge measurements were performed in the potential range of 0−0.5 V (vs Ag/AgCl) at a constant current density of 50 mA/g. Electrochemical impedance spectroscopy (EIS) tests were carried out by applying a sinusoidal potential perturbation at the open circuit potential with an amplitude of 10 mV. The impedance response was measured over frequencies between 1 MHz and 10 mHz, recording 6 points per decade of frequency. Impedance analysis was carried out using PAR ZSimpWin package for Windows generally for frequencies between 100 kHz and 50 mHz to prevent misinterpretation of any artifacts that may be present in the high-frequency region or scatter in the low-frequency region. The details of the fitting procedure to analyze the impedance data using electrical equivalent circuit is reported in the Supporting Information (section S3.2). The resistances reported in the work are normalized per unit gram of MOF material. All the electrochemical experiments were repeated at least thrice to examine the reproducibility of the electrochemical data.

3. RESULTS AND DISCUSSION

3.1. Material Synthesis. MOF-5 can be synthesized by various routes such as solvothermal,[31] direct mixing,[32] slow diffusion.[33] The synthesis route can control the crystallography and morphology of the resultant MOF crystals. Here, we adapted the "direct room temperature mixing approach", a fast synthesis method yielding bulk quantities of MOF. Ni doping of MOF-5 (MOF-5_{Ni}) has been previously reported by Li et al.[34] and Yang et al.[35] using the solvothermal method, but not by the direct room temperature mixing approach. In this report, the concentration of the doping content of Ni is based on the starting concentration of the precursor as the concentration of Ni in the filtered solution after the MOF had crystallized was negligible.

3.2. Characterization of Ni Doping of MOF-5 and Composite Formation with rGO. SEM micrographs (Figure 1a,b and Figure S2, Supporting Information) reveal that Ni doping did not alter the flake-like morphology of MOF-5. The flake dimensions in the longitudinal direction were in the range of 100−300 nm. Even the presence of rGO had little change on the overall morphology of the MOF crystals (Figure 1c−f). Discrete rGO nanosheets at low concentrations of rGO grew into continuous interconnected sheets (shown by arrows) at high concentration (~50%) of rGO (Figure 1f). A TEM micrograph (Figure 2b) providing clearer insight into the morphology of MOF-$5_{Ni50\%\ rGO50\%}$ shows that MOF crystals were randomly distributed on the rGO sheets. The EDX analysis (Figure S3c, Supporting Information) of the MOF crystals showed presence of both Ni and Zn in the MOF framework (Supporting Information, section S5).

Surface area and pore textural characterization suggested that rGO addition decreases the surface area of MOF (Table S1, Supporting Information), which is consistent with the literature.[20] The pore volume was marginally increased due to rGO addition (Table S1, Supporting Information), which can be attributed to the formation of new pore spaces at the MOF/rGO interfaces.[21] Details of the surface area and pore textural properties are reported in the Supporting Information (section S6).

XRD spectra of MOF-5 (Figure 3a) is analogous to simulated MOF-5 reported by Li et al.[34] and other reports,[27,28,32] but the intensity of the peak at 6.9° (*d* spacing, 12.8 Å)[36] is small in comparison to the peak at 9.7° (*d* spacing, 9.1 Å).[36] Prior reports have also demonstrated this anomaly in MOF-5 crystals.[27,28,32,36] Absence of any additional diffraction peak (Figure 3a) in MOF-5_{Ni} suggests it is iso-structural with MOF-5, which implies that Ni is incorporated into the framework by partial substitution of Zn ions in the $[Zn_4O]^{6+}$ clusters. This observation is consistent with the previous studies related to metal (Ni, Co) doping of MOF-5.[34,35,37] In the composite with rGO, the presence of rGO did not change the peak positions of MOF-$5_{Ni50\%}$ (Figure 3b), indicating that rGO did not hinder the formation of linkages between metal centers and organic ligands.[20] This also may suggest the formation of composites of rGO and MOF via weak electrostatic interaction in addition to other dispersive forces.[21] The peak around 26.5° arising from (002) plane of rGO coincides with a peak of MOF. However, Raman spectra of the MOF-$5_{Ni50\%\ rGO}$ composites confirmed the presence of rGO (Figure 3c). Graphitic structures including rGO (Figure 3c) are characterized by the G peak (~1590 cm^{-1}) assigned to the E_{2g} phonon of the sp^2 hybridization and the D peak (~1350 cm^{-1}), which is the breathing mode of κ-point phonons of A1g symmetry.[22,38] MOF-$5_{Ni50\%}$ is also Raman active due to the presence of terephthalic acid ligands with characteristic peaks at 1615, 1428, 1181, and 1138 cm^{-1} associated with the in-plane vibrational modes of the aromatic rings, while the peaks at 863 and 630 cm^{-1} correlate to C−H stretching or out-of-plane vibrational modes of the aromatic rings.[39] The characteristic peaks of both rGO and MOF-$5_{Ni50\%}$ were present in MOF-$5_{Ni50\%\ rGO}$ at their respective wave numbers, which further strengthens the formation of composites between rGO and MOF-5_{Ni}. We can see that rGO is more Raman active than MOF-$5_{Ni50\%}$, which is attributed to the larger number of aromatic rings in its structure, and as a result, a clear trend of the intensity of

DOI: 10.1021/am508119c
ACS Appl. Mater. Interfaces 2015, 7, 3655−3664

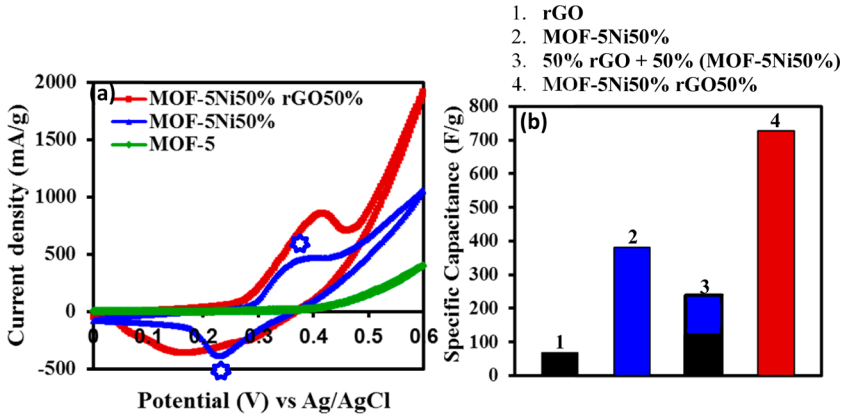

Figure 5. (a) Cyclic voltammetry of the MOF electrodes in 1 M KOH shows distinct redox peaks due to Ni doping in MOF-5. (b) Specific capacitance of rGO, MOF-$5_{Ni50\%}$ and MOF-$5_{Ni50\%\ rGO50\%}$. The measured specific capacitance of (red) MOF-$5_{Ni50\%\ rGO50\%}$ is around 3 fold larger than (blue + black) the algebraic sum of rGO and MOF-$5_{Ni50\%}$.

Table 1. Comparison of the Electrochemical Characteristics of MOF Electrodes in 1 M KOH

electrode	capacitance	charge transfer resistance (mΩ)	charge/discharge cyclability (%)	cycles required for complete activation	energy density	power density
MOF-5	90 F/g	184				
MOF-$5_{Ni50\%}$	380 F/g, 0.54 F/cm^2	74	195	260	19 Wh/kg, 2.67 × 10^{-5} Wh/cm^2	114 W/kg, 0.16 mW/cm^2
MOF-$5_{Ni50\%\ rGO50\%}$	758 F/g, 1.28 F/cm^2	6	214	65	37.8 Wh/kg, 6.41 × 10^{-5} Wh/cm^2	226.7 W/kg, 0.4 mW/cm^2

graphitic peaks with rGO content is not observed. However, the peak at 863 cm^{-1} from MOF-$5_{Ni50\%}$ decreases in intensity as the content of rGO increases. We also draw attention to the presence of a broad 2D band in these composites; the 2D-to-G ratio of graphene layers is 0.2 ± 0.02, which corresponds to 3−4 layers of rGO.[40] This suggests that rGO in the composite is nicely exfoliated and, to a large extent, protected from restacking by the MOF crystals as these rGO sheets form a thin membrane like structure on which the MOF crystals were distributed (Figures 1c−f and 2b).

3.3. Effect of Ni and rGO on Electrochemical Properties of MOF-5. We have restricted our studies to Ni doping concentration of 50% as higher concentrations are likely to change the crystal structure of the parent MOF-5. The capacitance of MOF-5 measured from CV plots (Figure S8a, Supporting Information) increased with increasing Ni doping concentrations (Figure 4a), which is not surprising given the increase in the number of redox sites. The capacitance ∼380 F/g at 50% Ni doping concentration is similar to Co based MOF (∼206.76 F/g) in 0.5 M lithium hydroxide (LiOH))[17] but larger than Co doped MOF 5 (3.5 F/g) in $TBSPF_6$ in acetonitrile[18] highlighting the consequence of participation of redox active metal centers. Even the areal capacitance of MOF-$5_{Ni50\%}$ (534 mF/cm^2) was significantly higher than recent reports of nHKUST-1 MOF (0.324 mF/cm^2 in 1 M tetraethylammonium tetrafluoroborate) reported by Choi et al.[24] These results suggest that doping existing MOFs with redox active metal centers engaged in reversible redox reactions is a practical approach for increasing the charge storage in MOFs. Charge storage capability further improved when composites were formed with rGO (Figure 4b). The impact of rGO addition on capacitance (calculated from Figure S10a, Supporting Information) is minimal at low concentration of rGO (5 and 10%), but increases dramatically with increasing rGO (30 and 50%). Maximum capacitance as high as 758 F/g was achieved in case of MOF-$5_{Ni50\%\ rGO50\%}$, as at a concentration of 50%, rGO starts forming an interconnected membrane-like structure (Figures 1f and 2b). When these values are converted to areal capacitance (∼1.28 F/cm^2) the metrics are seemingly larger than most published reports of MOF rGO composites.[24]

3.4. Comparison of MOF-$5_{Ni50\%}$ and MOF-$5_{Ni50\%\ rGO50\%}$. Although various compositions were prepared and studied, here, we will compare and contrast two representative compositions: MOF-$5_{Ni50\%}$ and MOF-$5_{Ni50\%\ rGO50\%}$. Redox peaks with distinguishable cathodic and anodic peaks separated by ∼122 mV were observed in MOF-$5_{Ni50\%}$, whereas MOF-$5_{Ni50\%\ rGO50\%}$ shows an anodic peak and a broad cathodic response (Figure 5a). The broad cathodic response is suggestive of double layer charging behavior from the rGO nanosheets which masks the Faradaic response. In Figure 5b, we highlight that the measured capacitance of MOF-$5_{Ni50\%\ rGO50\%}$ (758 F/g) is around 3 fold higher than the algebraic sum of the constituents (224 F/g), if one considers equal contributions from electrical double layer charging in rGO and Faradaic reactions in MOF-$5_{Ni50\%}$. This can be attributed to a synergetic interaction between rGO and MOF[41,42] and not merely a physical composite as evidenced by the enhanced current response of the Faradaic anodic peak in MOF-$5_{Ni50\%\ rGO50\%}$. A broad overview of the electrochemical properties of relevant materials is shown in Table 1.

3.5. Mechanism of Redox Reactions in Ni-Doped MOF 5 and Cyclability. In general, significant morphological and chemical changes occur in electrodes undergoing Faradaic redox reactions, which often results in limited cyclability,[43] but Table 1 reports the unusually large cyclability (>100%) for our MOF materials. This raises the questions: What are the possible redox reactions occurring from Ni doping? Are these reactions reversible? What chemical and morphological changes occur due to these reactions? To answer these questions, we

DOI: 10.1021/am508119c
ACS Appl. Mater. Interfaces 2015, 7, 3655−3664

investigated MOF-$5_{Ni50\%}$ electrodes by SEM and XRD right after the oxidation peak and again right after the reduction peak (represented by the stars in Figure 5a) after five cycles of CV at a scan rate of 1 mV/s. The surface of the electrode after oxidation was covered with oxide particles (Figure 6b), but they disappeared after reduction (Figure 6c) and resembled the parent electrode (Figure 6a). XRD spectra (Figure 6d) of the electrode collected after oxidation had distinct peaks at 14.4, 24.5, 28.8, 34.4, and 39.5° and confirmed the presence of nickel hydroxide, $Ni(OH)_2$, (PDF No. 0.38-0.715 and PDF No. 014-0117),[44,45] which vanished after reduction. The XRD spectrum of the original MOF is therefore restored in agreement with the morphological changes shown in Figures 6a–c. We propose that Ni metal centers in MOF-5 undergo a 2-electron redox reaction based on existing reports on Faradaic redox reactions at Ni surface in alkaline electrolytes.[46,47]

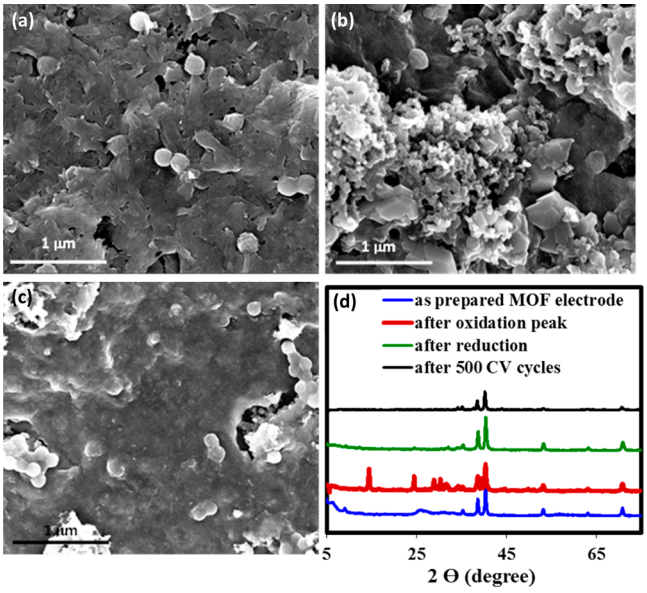

Figure 6. SEM images of MOF-$5_{Ni50\%}$ electrode morphologies; (a) as -prepared, (b) after oxidation, and (c) after reduction. (d) XRD shows the prominent $Ni(OH)_2$ peaks after oxidation and their disappearance after reduction.

$$Ni + 2OH^- \leftrightarrow Ni(OH)_2 + 2e^-$$

In a reversible redox reaction, the potential difference between the redox peaks is 59 mV n^{-1}, where n is the number of electrons involved.[48,49] Astonishingly, the redox peak separation is ~122 mV (Figure 5a) which strongly reinforces the two electron mechanism. Unlike the Ni surfaces in alkaline electrolytes the reaction is highly reversible (Figure S9a, Supporting Information) because the Ni sites are stabilized in the MOF structure by the terephthalic acid ligands and reverts back to the parent MOF structure after redox cycling is completed. We believe this efficient two-electron redox reaction at the Ni sites of doped MOF-5 distinguishes our composite material from the rather extensively studied Ni oxide/hydroxide pseudocapacitors[41,50] which undergo a one-electron transfer between $Ni(OH)_2$ and NiO(OH) phases. Furthermore, little change in the XRD spectra (Figure 6d) of the as-made MOF-$5_{Ni50\%}$ electrode and one collected after 500 cycles of CV along with the recurring CV plots (Figure S9a, Supporting Information) reinforces the reversibility of Ni doped MOF-5 system. Galvanostatic charge/discharge cycling of MOF-$5_{Ni50\%}$ and MOF-$5_{Ni50\%\ rGO50\%}$ in Figure 7a shows that the specific capacitance of MOF grows with increased cycling and the capacitance reaches a plateau as the electrolyte slowly and steadily diffuses through the highly porous MOF structure to gradually activate the redox active sites.[51] This behavior has not been observed in $Ni(OH)_2$/rGO composite[52] and in part explains the larger than 100% cyclability.

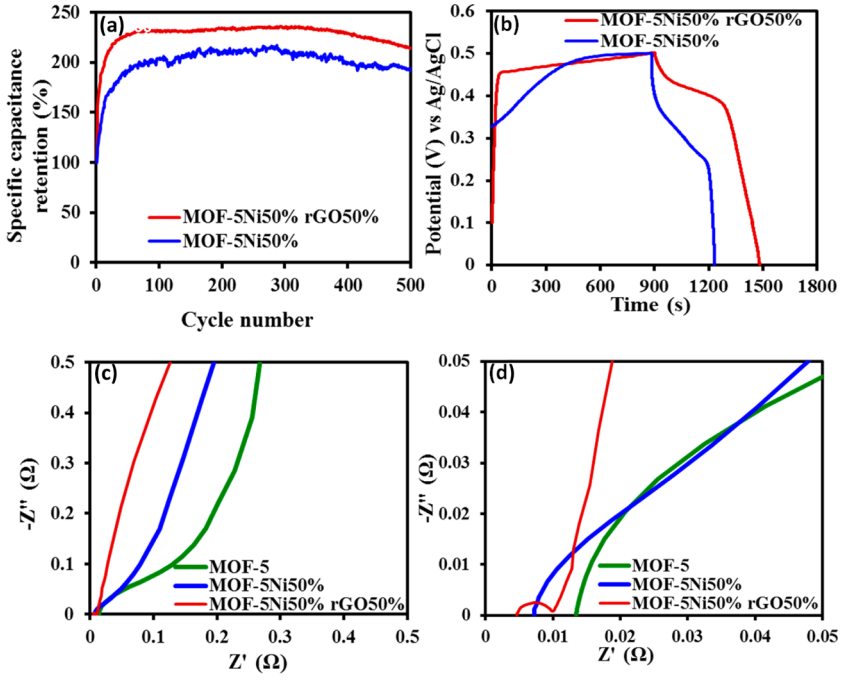

Figure 7. (a) Excellent specific capacitance retention for MOF-$5_{Ni50\%\ rGO50\%}$ and MOF-$5_{Ni50\%}$. (b) Slower discharge rate with a smaller *iR* drop from rGO addition to MOF-$5_{Ni50\%}$. (c) Nyquist plots and (d) magnified view of the boxed section of (c) showing the charge transfer resistance.

DOI: 10.1021/am508119c
ACS Appl. Mater. Interfaces 2015, 7, 3655–3664

3.6. Effect of Decrease in Charge Transfer Resistance from Electron Conducting rGO. The nonlinear discharge plots (Figure 7b) are typical of those reported[41,50,53,54] for systems undergoing crystallographic transformations from Faradaic redox reactions.[49] Addition of rGO in this system clearly decreases the resistive *iR* drop (Figure 7b) in the discharge curves for MOF-$5_{Ni50\%\ rGO50\%}$ (~2 mV) over MOF-$5_{Ni50\%}$ (~60 mV) in direct agreement with the electrical conductivity measurements (Figure S5, Supporting Information).

The enhanced charge transport kinetics due to rGO addition observed from CV and galvanostatic charge/discharge experiments is elucidated by electrochemical impedance spectroscopy (EIS) as shown in Figures 7c,d. The employed electrical equivalent circuit (EEC) consists of two time constants connected in series (Figure S11, Supporting Information), each comprising of a constant phase element (Q) and a resistance (R). The first time constant represents the charge transfer processes, while the second time constant represents mass transfer. The fitting procedure, comparison of the simulated, and the experimentally obtained impedance data, related error plots and the calculated parameters (Rs, Q_1, R_1, Q_2, and R_2) are elaborated in the Supporting Information (sections S3.2 and S12). Charge transfer resistance (R_1) determines the charge transport kinetics at the electrode/electrolyte interface, and a decrease in the charge transfer resistance would lead to an enhanced electrochemical response of the system.[55] The charge transfer resistances of ~184 mΩ for MOF-5 and ~74 mΩ for MOF-$5_{Ni50\%}$ highlight the heightened charge transfer by Faradaic reactions of Ni and corroborate with enhanced currents in the CV measurements. The charge transfer resistance of ~6 mΩ for MOF-$5_{Ni50\%\ rGO50\%}$ is more than 1 order of magnitude smaller than MOF-$5_{Ni50\%}$ as charge transfer is facilitated through the electronically conducting graphene nanosheets, which act as efficient conduits by connecting the distributed redox species in the MOF crystals. Given that the Nyquist plot (Figure 7d) and CV (Figure 5a) indicate that electrochemical double layer charging are also at play in MOF-$5_{Ni50\%\ rGO50\%}$, the charge transfer mechanism in MOF-$5_{Ni50\%\ rGO50\%}$ is complex and involves double layer charging, Faradaic reactions and efficient transport of redox generated charges. Additions of Ni and rGO, however, do not change the mass transfer resistance (Table S2, Supporting Information, column R_2) of MOF-5 highlighting that the mesoporous structure is not significantly modified by our two-pronged strategy. The lowered charge transfer resistance without adverse effects on the mass transfer resistance from rGO inclusion roughly doubles both the energy and the power density in MOF-$5_{Ni50\%\ rGO50\%}$ over MOF-$5_{Ni50\%}$, as shown in Table 1. An estimation of the energy and power densities with a view to assess the potential of MOF-$5_{Ni50\%\ rGO50\%}$ as an energy storage material reveals energy density of 37.8 Wh/kg (6.41×10^{-5} Wh/cm^2) at a power density of 227 W/kg (0.4 mW/cm^2), which is comparable to Ni-hydroxide-based pseudocapacitors.[50]

4. CONCLUSIONS

Incorporation of Ni ions in the MOF-5 framework via partial substitution of Zn ions in the $[Zn_4O]^{6+}$ clusters introduces efficient, reversible, two-electron Faradaic redox reactions in the presence of an alkaline electrolyte. The reaction reported here for the first time dramatically improves the charge storage capability of the MOF. The addition of a conductive phase in the form of rGO significantly reduces the charge transfer resistance, decreases the ESR, improves the power delivery, and enhances the electrochemical capacitance of the system. The capacitance of this composite is almost 3 times larger than the algebraic sum of contributions from the Faradaic capacitance of Ni-doped MOF-5 and double-layer capacitance of rGO. An efficient charge transfer process from the synergy between the interconnected graphene nanosheets and distributed Ni centers in the MOF-5 realizes materials with energy density of 37.8 Wh/kg at a power density of 226.7 W/kg and large stability during cycling. These metrics are comparable to current literature standards in Ni-hydroxide-based supercapacitors.[50] Further improvements are possible through the incorporation of multiple dopant ions to participate in redox reactions across a larger voltage range. Our study establishes a general two-pronged strategy through transition metal doping and incorporation of conductive phases to transform a prototypical MOF to a high-performance energy storage material. These results will instigate further research across the wide family of MOFs known today as tunable energy storage and delivery materials.

■ ASSOCIATED CONTENT

Supporting Information

Procedure for graphene oxide (GO) synthesis, details of electrical conductivity measurements, parametric calculations and data analysis, SEM micrographs of MOF-5 doped with 10% and 30% Ni, TEM and EDX analysis of MOF-$5_{Ni50\%}$ and MOF-$5_{Ni50\%\ rGO50\%}$, surface area and pore textural characterization of MOF-$5_{Ni50\%}$ and MOF-$5_{Ni50\%\ rGO50\%}$, electrical conductivity of MOF-$5_{Ni50\%\ rGO}$ as a function of rGO concentration, electrical responses of Ti current collector, rGO, MOF-5 electrodes due to Ni addition and MOF-$5_{Ni50\%}$ due to rGO addition, and EIS data analysis using an electrical equivalent circuit. This material is available free of charge via the Internet at http://pubs.acs.org.

■ AUTHOR INFORMATION

Corresponding Author

*E-mail: mainak.majumder@monash.edu.

Notes

The authors declare no competing financial interest.

■ ACKNOWLEDGMENTS

The authors gratefully acknowledge support from the Linkage Scheme of the Australian Research Council (LP110100612), partner investigator Strategic Energy Resources and their wholly owned subsidiary, Ionic Industries, Pty., Ltd., and the Monash Center for Electron Microscopy.

■ REFERENCES

(1) Conway, B. E. *Electrochemical Supercapacitors, Scientific Fundamentals and Technological Applications*. Plenum Press: New York, 1999.

(2) Farha, O. K.; Eryazici, I.; Jeong, N. C.; Hauser, B. G.; Wilmer, C. E.; Sarjeant, A. A.; Snurr, R. Q.; Nguyen, S. T.; Yazaydın, A. Ö.; Hupp, J. T. Metal−Organic Framework Materials with Ultrahigh Surface Areas: Is the Sky the Limit? *J. Am. Chem. Soc.* **2012**, *134*, 15016−15021.

(3) Rowsell, J. L. C.; Yaghi, O. M. Metal Organic Frameworks: A New Class of Porous Materials. *Microporous Mesoporous Mater.* **2004**, *73*, 3−14.

(4) Kitagawa, S.; Kitaura, R.; Noro, S.-I. Functional Porous Coordination Polymers. *Angew. Chem., Int. Ed.* **2004**, *43*, 2334−2375.

(5) Majumder, M.; Sheath, P.; Mardel, J. I.; Harvey, T. G.; Thornton, A. W.; Gonzago, A.; Kennedy, D. F.; Madsen, I.; Taylor, J. W.; Turner,

DOI: 10.1021/am508119c
ACS Appl. Mater. Interfaces 2015, 7, 3655−3664

D. R.; Hill, M. R. Aqueous Molecular Sieving and Strong Gas Adsorption in Highly Porous MOFs with a Facile Synthesis. *Chem. Mater.* **2012**, *24*, 4647−4652.
(6) Corma, A.; García, H.; Llabrés i Xamena, F. X. Engineering Metal Organic Frameworks for Heterogeneous Catalysis. *Chem. Rev.* **2010**, *110*, 4606−4655.
(7) Czaja, A. U.; Trukhan, N.; Muller, U. Industrial Applications of Metal−Organic Frameworks. *Chem. Soc. Rev.* **2009**, *38*, 1284−1293.
(8) Ferey, G. Hybrid Porous Solids: Past, Present, Future. *Chem. Soc. Rev.* **2008**, *37*, 191−214.
(9) Horcajada, P.; Serre, C.; Maurin, G.; Ramsahye, N. A.; Balas, F.; Vallet-Regí, M. A.; Sebban, M.; Taulelle, F.; Férey, G. R. Flexible Porous Metal−Organic Frameworks for a Controlled Drug Delivery. *J. Am. Chem. Soc.* **2008**, *130*, 6774−6780.
(10) Horcajada, P.; Chalati, T.; Serre, C.; Gillet, B.; Sebrie, C.; Baati, T.; Eubank, J. F.; Heurtaux, D.; Clayette, P.; Kreuz, C.; Chang, J.-S.; Hwang, Y. K.; Marsaud, V.; Bories, P.-N.; Cynober, L.; Gil, S.; Ferey, G.; Couvreur, P.; Gref, R. Porous Metal−Organic-Framework Nanoscale Carriers as a Potential Platform for Drug Delivery and Imaging. *Nat. Mater.* **2010**, *9*, 172−178.
(11) Kreno, L. E.; Leong, K.; Farha, O. K.; Allendorf, M.; Van Duyne, R. P.; Hupp, J. T. Metal−Organic Framework Materials as Chemical Sensors. *Chem. Rev.* **2011**, *112*, 1105−1125.
(12) Scholz, F.; Meyer, B. *Electroanalytical Chemistry*. Marcel Dekker: New York, 1998; Vol. *20*.
(13) Dutta, P. K.; Ledney, M. Charge-Transfer Processes in Zeolites: Toward Better Artificial Photosynthetic Models. In *Progress in Inorganic Chemistry*, Meyer, G. J., Ed. John Wiley & Sons, Inc.: 2007; pp 209−271.
(14) Rolison, D. R.; Bessel, C. A. Electrocatalysis and Charge-Transfer Reactions at Redox-Modified Zeolites. *Acc. Chem. Res.* **2000**, *33*, 737−744.
(15) Doménech, A.; García, H.; Doménech-Carbó, M. T.; Llabrés-i-Xamena, F. Electrochemistry of Metal−Organic Frameworks: A Description from the Voltammetry of Microparticles Approach. *J. Phys. Chem. C* **2007**, *111*, 13701−13711.
(16) Loera-Serna, S.; Oliver-Tolentino, M. A.; de Lourdes López-Núñez, M.; Santana-Cruz, A.; Guzmán-Vargas, A.; Cabrera-Sierra, R.; Beltrán, H. I.; Flores, J. Electrochemical Behavior of $[Cu_3(BTC)_2]$ Metal−Organic Framework: The Effect of the Method of Synthesis. *J. Alloys Compd.* **2012**, *540*, 113−120.
(17) Lee, D. Y.; Yoon, S. J.; Shrestha, N. K.; Lee, S.-H.; Ahn, H.; Han, S.-H. Unusual Energy Storage and Charge Retention in Co-Based Metal−Organic-Frameworks. *Microporous Mesoporous Mater.* **2012**, *153*, 163−165.
(18) Díaz, R.; Orcajo, M. G.; Botas, J. A.; Calleja, G.; Palma, J. Co8-MOF-5 as Electrode for Supercapacitors. *Mater. Lett.* **2012**, *68*, 126−128.
(19) Stoller, M. D.; Park, S.; Zhu, Y.; An, J.; Ruoff, R. S. Graphene-Based Ultracapacitors. *Nano Lett.* **2008**, *8*, 3498−3502.
(20) Petit, C.; Bandosz, T. J. MOF−Graphite Oxide Composites: Combining the Uniqueness of Graphene Layers and Metal−Organic Frameworks. *Adv. Mater.* **2009**, *21*, 4753−4757.
(21) Petit, C.; Mendoza, B.; Bandosz, T. J. Reactive Adsorption of Ammonia on Cu-Based MOF/Graphene Composites. *Langmuir* **2010**, *26*, 15302−15309.
(22) Guo, Y.; Han, Y.; Shuang, S.; Dong, C. Rational Synthesis of Graphene-Metal Coordination Polymer Composite Nanosheet as Enhanced Materials for Electrochemical Biosensing. *J. Mater. Chem.* **2012**, *22*, 13166−13173.
(23) Guo, Z.; Reddy, M. V.; Goh, B. M.; San, A. K. P.; Bao, Q.; Loh, K. P. Electrochemical Performance of Graphene and Copper Oxide Composites Synthesized From a Metal−Organic Framework (Cu-MOF). *RSC Adv.* **2013**, *3*, 19051−19056.
(24) Choi, K. M.; Jeong, H. M.; Park, J. H.; Zhang, Y.-B.; Kang, J. K.; Yaghi, O. M. Supercapacitors of Nanocrystalline Metal−Organic Frameworks. *ACS Nano* **2014**, *8*, 7451−7457.
(25) Pourbaix, M. Atlas of Electrochemical Equilibria in Aqueous Solutions. National Association of Corrosion Engineers: Houston, TX, 1974.
(26) Li, H.; Eddaoudi, M.; O'Keeffe, M.; Yaghi, O. M. Design and Synthesis of an Exceptionally Stable and Highly Porous Metal−Organic Framework. *Nature* **1999**, *402*, 276−279.
(27) Saha, D.; Deng, S.; Yang, Z. Hydrogen Adsorption on Metal−Organic Framework (MOF-5) Synthesized by DMF Approach. *J. Porous Mater.* **2009**, *16*, 141−149.
(28) Panella, B.; Hirscher, M. Hydrogen Physisorption in Metal−Organic Porous Crystals. *Adv. Mater.* **2005**, *17*, 538−541.
(29) Kovtyukhova, N. I.; Ollivier, P. J.; Martin, B. R.; Mallouk, T. E.; Chizhik, S. A.; Buzaneva, E. V.; Gorchinskiy, A. D. Layer-by-Layer Assembly of Ultrathin Composite Films from Micron-Sized Graphite Oxide Sheets and Polycations. *Chem. Mater.* **1999**, *11*, 771−778.
(30) Stankovich, S.; Dikin, D. A.; Piner, R. D.; Kohlhaas, K. A.; Kleinhammes, A.; Jia, Y.; Wu, Y.; Nguyen, S. T.; Ruoff, R. S. Synthesis of Graphene-Based Nanosheets Via Chemical Reduction of Exfoliated Graphite Oxide. *Carbon* **2007**, *45*, 1558−1565.
(31) Hafizovic, J.; Bjørgen, M.; Olsbye, U.; Dietzel, P. D. C.; Bordiga, S.; Prestipino, C.; Lamberti, C.; Lillerud, K. P. The Inconsistency in Adsorption Properties and Powder XRD Data of MOF-5 Is Rationalized by Framework Interpenetration and the Presence of Organic and Inorganic Species in the Nanocavities. *J. Am. Chem. Soc.* **2007**, *129*, 3612−3620.
(32) Huang, L.; Wang, H.; Chen, J.; Wang, Z.; Sun, J.; Zhao, D.; Yan, Y. Synthesis, Morphology Control, and Properties of Porous Metal−Organic Coordination Polymers. *Microporous Mesoporous Mater.* **2003**, *58*, 105−114.
(33) Li, H.; Eddaoudi, M.; Groy, T. L.; Yaghi, O. M. Establishing Microporosity in Open Metal−Organic Frameworks: Gas Sorption Isotherms for Zn(BDC) (BDC = 1,4-Benzenedicarboxylate). *J. Am. Chem. Soc.* **1998**, *120*, 8571−8572.
(34) Li, H.; Shi, W.; Zhao, K.; Li, H.; Bing, Y.; Cheng, P. Enhanced Hydrostability in Ni-Doped MOF-5. *Inorg. Chem.* **2012**, *51*, 9200−9207.
(35) Yang, J.-M.; Liu, Q.; Sun, W.-Y. Shape and Size Control and Gas Adsorption of Ni(II)-Doped MOF-5 Nano/Microcrystals. *Microporous Mesoporous Mater.* **2014**, *190*, 26−31.
(36) Hafizovic, J.; Bjørgen, M.; Olsbye, U.; Dietzel, P. D. C.; Bordiga, S.; Prestipino, C.; Lamberti, C.; Lillerud, K. P. The Inconsistency in Adsorption Properties and Powder XRD Data of MOF-5 Is Rationalized by Framework Interpenetration and the Presence of Organic and Inorganic Species in the Nanocavities. *J. Am. Chem. Soc.* **2007**, *129*, 3612−3620.
(37) Botas, J. A.; Calleja, G.; Sánchez-Sánchez, M.; Orcajo, M. G. Cobalt Doping of the MOF-5 Framework and Its Effect on Gas-Adsorption Properties. *Langmuir* **2010**, *26*, 5300−5303.
(38) Das, A.; Pisana, S.; Chakraborty, B.; Piscanec, S.; Saha, S. K.; Waghmare, U. V.; Novoselov, K. S.; Krishnamurthy, H. R.; Geim, A. K.; Ferrari, A. C.; Sood, A. K. Monitoring Dopants by Raman Scattering in an Electrochemically Top-Gated Graphene Transistor. *Nat. Nanotechnol.* **2008**, *3*, 210−215.
(39) Bordiga, S.; Lamberti, C.; Ricchiardi, G.; Regli, L.; Bonino, F.; Damin, A.; Lillerud, K. P.; Bjørgen, M.; Zecchina, A. Electronic and Vibrational Properties of a MOF-5 Metal−Organic Framework: ZnO Quantum Dot Behaviour. *Chem. Commun.* **2004**, *20*, 2300−2301.
(40) Kim, K. S.; Zhao, Y.; Jang, H.; Lee, S. Y.; Kim, J. M.; Kim, K. S.; Ahn, J.-H.; Kim, P.; Choi, J.-Y.; Hong, B. H. Large-Scale Pattern Growth of Graphene Films for Stretchable Transparent Electrodes. *Nature* **2009**, *457*, 706−710.
(41) Wang, H.; Casalongue, H. S.; Liang, Y.; Dai, H. $Ni(OH)_2$ Nanoplates Grown on Graphene as Advanced Electrochemical Pseudocapacitor Materials. *J. Am. Chem. Soc.* **2010**, *132*, 7472−7477.
(42) Yan, J.; Fan, Z.; Wei, T.; Qian, W.; Zhang, M.; Wei, F. Fast and Reversible Surface Redox Reaction of Graphene-MnO_2 Composites as Supercapacitor Electrodes. *Carbon* **2010**, *48*, 3825−3833.
(43) Yu, G.; Hu, L.; Vosgueritchian, M.; Wang, H.; Xie, X.; McDonough, J. R.; Cui, X.; Cui, Y.; Bao, Z. Solution-Processed

DOI: 10.1021/am508119c
ACS Appl. Mater. Interfaces 2015, 7, 3655−3664

Graphene/MnO_2 Nanostructured Textiles for High-Performance Electrochemical Capacitors. *Nano Lett.* **2011**, *11*, 2905−2911.
(44) Jeevanandam, P.; Koltypin, Y.; Gedanken, A. Synthesis of Nanosized α-Nickel Hydroxide by a Sonochemical Method. *Nano Lett.* **2001**, *1*, 263−266.
(45) Xu, L.; Ding, Y.-S.; Chen, C.-H.; Zhao, L.; Rimkus, C.; Joesten, R.; Suib, S. L. 3D Flowerlike α-Nickel Hydroxide with Enhanced Electrochemical Activity Synthesized by Microwave-Assisted Hydrothermal Method. *Chem. Mater.* **2007**, *20*, 308−316.
(46) van Drunen, J.; Kinkead, B.; Wang, M. C. P.; Sourty, E.; Gates, B. D.; Jerkiewicz, G. Comprehensive Structural, Surface-Chemical and Electrochemical Characterization of Nickel-Based Metallic Foams. *ACS Appl. Mater. Interfaces* **2013**, *5*, 6712−6722.
(47) Hall, D. S.; Bock, C.; MacDougall, B. R. The Electrochemistry of Metallic Nickel: Oxides, Hydroxides, Hydrides, and Alkaline Hydrogen Evolution. *J. Electrochem. Soc.* **2013**, *160*, F235−F243.
(48) Bard, A. J.; Faulkner, L. R. *Electrochemical Methods: Fundamentals and Applications*. John Wiley & Sons, Inc.: New York, 2001.
(49) Augustyn, V.; Simon, P.; Dunn, B. Pseudocapacitive Oxide Materials for High-Rate Electrochemical Energy Storage. *Energy Environ. Sci.* **2014**, *7*, 1597−1614.
(50) Li, H. B.; Yu, M. H.; Wang, F. X.; Liu, P.; Liang, Y.; Xiao, J.; Wang, C. X.; Tong, Y. X.; Yang, G. W. Amorphous Nickel Hydroxide Nanospheres with Ultrahigh Capacitance and Energy Density as Electrochemical Pseudocapacitor Materials. *Nat. Commun.* **2013**, *4*, 1−7.
(51) Wei, T.-Y.; Chen, C.-H.; Chien, H.-C.; Lu, S.-Y.; Hu, C.-C. A Cost-Effective Supercapacitor Material of Ultrahigh Specific Capacitances: Spinel Nickel Cobaltite Aerogels from an Epoxide-Driven Sol−Gel Process. *Adv. Mater.* **2010**, *22*, 347−351.
(52) Xiao, J.; Yang, S. Nanocomposites of $Ni(OH)_2$/Reduced Graphene Oxides with Controllable Composition, Size, and Morphology: Performance Variations as Pseudocapacitor Electrodes. *ChemPlusChem.* **2012**, *77*, 807−816.
(53) Zhang, L. L.; Xiong, Z.; Zhao, X. S. A Composite Electrode Consisting of Nickel Hydroxide, Carbon Nanotubes, and Reduced Graphene Oxide with an Ultrahigh Electrocapacitance. *J. Power Sources* **2013**, *222*, 326−332.
(54) Yang, G.-W.; Xu, C.-L.; Li, H.-L. Electrodeposited Nickel Hydroxide on Nickel Foam with Ultrahigh Capacitance. *Chem. Commun.* **2008**, *48*, 6537−6539.
(55) Singh, A. K.; Sarkar, D.; Gopal Khan, G.; Mandal, K. Designing One Dimensional Co-Ni/Co_3O_4−NiO Core/Shell Nano-Heterostructure Electrodes for High-Performance Pseudocapacitor. *Appl. Phys. Lett.* **2014**, *104*, 133904−1−133904−4.

DOI: 10.1021/am508119c
ACS Appl. Mater. Interfaces 2015, 7, 3655−3664